Ultrafast Molecule Separation through Layered WS_2 Nanosheet Membranes

Luwei Sun,[†] Yulong Ying,[†] Hubiao Huang,[†] Zhigong Song,[‡] Yiyin Mao,[†] Zhiping Xu,[‡] and Xinsheng Peng[†,§,*]

[†]State Key Laboratory of Silicon Materials, Department of Materials Science and Engineering, Zhejiang University, Hangzhou 310027, China, [‡]Applied Mechanics Laboratory, Department of Engineering Mechanics and Center for Nano and Micro Mechanics, Tsinghua University, Beijing 100084, China, and [§]Cyrus Tang Centre for Sensor Materials and Applications, Zhejiang University, Hangzhou 310027, China

ABSTRACT Two-dimensional layered materials have joined in the family of size-selective separation membranes recently. Here, chemically exfoliated tungsten disulfide (WS_2) nanosheets are assembled into lamellar thin films and explored as an ultrafast separation membrane for small molecules with size of about 3 nm. Layered WS_2 membranes exhibit 5- and 2-fold enhancement in water permeance of graphene oxide membranes and MoS_2 laminar membranes with similar rejection, respectively. To further increase the water permeance, ultrathin nanostrands are used as templates to generate more fluidic channel networks in the WS_2 membrane. The water permeation behavior and separation performance in the pressure loading−unloading process reveal that the channels created by the ultrathin nanostrands are cracked under high pressure and result in a further 2-fold increase of the flux without significantly degrading the rejection for 3 nm molecules. This is supported by finite-element-based mechanical simulation. These layered WS_2 membranes demonstrate up to 2 orders of magnitude higher separation performance than that of commercial membranes with similar rejections and hold the promising potential for water purification.

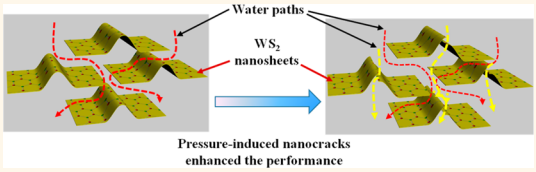

KEYWORDS: layered materials · tungsten disulfide · separation membrane · nanostrands

Functional membranes used for selective molecule separation in the modern water purification industry are extensively developed.[1,2] With the industry era coming, dramatic population growth and severe environmental pollution force researchers to develop effective strategies for obtaining clean air and water sources.[3] In earlier stages, the diffusion mechanism governs the performance of the dense polymer separation membranes.[4] Afterward, various porous materials like zeolites,[5] porous polymers,[6] and metal organic frameworks[7] are used in size-selective separation. Recently, graphene oxide (GO) membranes are found to enable water vapor permeation through ~1 nm graphene capillary networks constructed by oxygen-containing functionalized groups that enlarge the interspaces between the GO layers.[8] Their selective separation performances are afterward investigated in detail.[9] Excluding molecules by size from liquid is another application for GO membranes. The corrugations in GO membranes are used to block metal nanoparticles with several nanometers.[10] Very recently, flexible ultrathin nanostrands are explored to generate more nanochannels in the GO membranes,[11] which exhibit ultrafast viscous water flow and excellent separation performance for 3 nm molecules. These works indicate that two-dimensional layered materials can be expected as new materials for novel separation membranes.

As the analogue of graphene, a series of two-dimensional (2D) layered materials are developed.[12,13] The physics and chemistry of the 2D layered materials are concentrated in order to expand their applications in transistors,[14] photodetectors,[15] optics,[16] lithium ion batteries,[17] catalysts,[18,19] and sensors.[20] Although tens of novel 2D layered materials are found,[21] the separation membranes made of them are rather scarce, except recently for MoS_2[22] and GO nanosheets.[8−11,23] Like graphene and its derivatives,[24,25] layered transition-metal dichalcogenides have also desirable mechanical properties[26−28] and could be assembled into lamellar thin films. Therefore, they are expected to be used to construct novel high-performance lamellar separation membranes.

Herein, highly efficient size-selective separation membranes are assembled from chemically exfoliated WS_2 nanosheets by filtration. The as-prepared WS_2 membrane demonstrates a water permeance of 450 $L/m^2 \cdot h \cdot bar$ with over 90% rejection for 3 nm Evans Blue

* Address correspondence to pengxinsheng@zju.edu.cn.

Received for review April 1, 2014 and accepted May 22, 2014.

Published online May 22, 2014
10.1021/nn501786m

(EB) molecules. The water permeance is further improved to 930 L/m^2·h·bar by employing ultrathin metal hydroxide nanostrands as templates to generate more nanochannels between the WS_2 sheets, without degradation of the rejection property. These performances are up to 2 orders of magnitude higher than that of commercial membranes with similar rejections.[11] According to the water permeation behavior during the pressure loading−unloading process, we suggest that the regular nanochannels generated by nanostrands are likely cracked under high pressure, while the original irregular corrugations of WS_2 nanosheets are not. Surprisingly, the cracked nanochannels provide additional water entrance and remarkably increase the water permeance without losing the rejection. These novel WS_2 membranes are expected for new ultrafast separation membranes for water purification.

RESULTS AND DISCUSSION

The chemically exfoliated WS_2 nanosheets are prepared as previously reported[19] (see details in Materials and Methods). Diluted WS_2 nanosheet dispersion (0.2 mg/mL) is used to prepare the WS_2 nanosheet membranes by filtration. The XRD patterns recorded from the as-prepared WS_2 membrane (Figure 1a) coincide well with that of the standard PDF card of WS_2 (JCPDF No. 08-0237). An obvious peak at 14.5° results from the (002) plane in the hexagonal WS_2 structure. No other phase is observed. The AFM image (Figure 1b) shows that the thickness of a single WS_2 sheet is about 1.25 nm, close to an atomically thick WS_2 single layer sheet.[15] The lateral dimension is at micrometer scale, although several small fractured pieces, around hundreds of nanometers, are observed. Some corrugations are observed in the overview SEM image of the membrane (Figure 1c), like those appearing in GO and MoS_2 nanosheets.[10,22,23] These corrugations are established during the membrane formation process. The cross-section image (Figure 1d) shows that the thickness of the membrane is about 500 nm. The individual WS_2 nanosheets are interlocked with each other in a parallel manner and form lamellar structures during the vacuum filtration process.

In order to obtain a highly efficient separation membrane, the membrane should have a proper thickness to balance water flux and rejection rate. Too thick membrane has low water flux despite high rejection rate, while a thinner membrane usually presents higher flux but worse rejection and suffers mechanical problems.[1] The thickness-dependent separation performances of WS_2 membranes are shown in Figure 2a. The thickness of the membranes is controlled by the volume of the WS_2 nanosheet dispersion. The water permeance is 2-fold enhanced with the thickness decreasing from 1500 to 300 nm. EB (1.2 nm × 3.1 nm) and cytochrome *c* (cyt *c*, 2.5 nm × 3.7 nm)

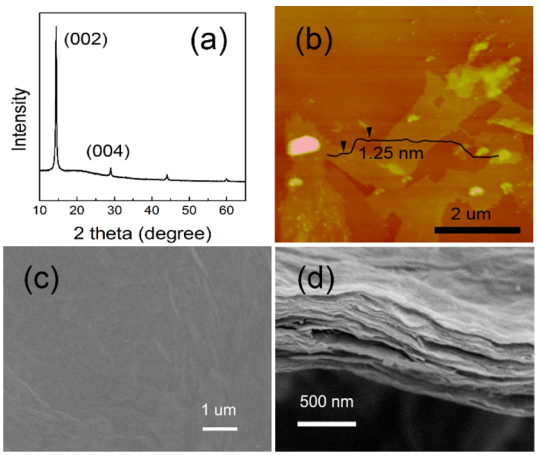

Figure 1. Crystal phase and morphology characterization of WS_2 nanosheets and membranes. (a) XRD pattern; (b) AFM image of WS_2 nanosheets; (c) typical overview; and (d) cross-sectional SEM image of WS_2 membrane with a thickness of 500 nm.

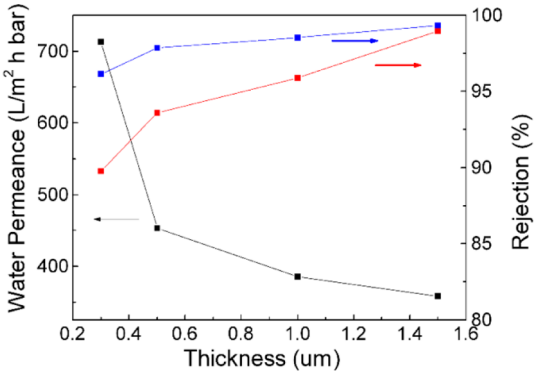

Figure 2. Thickness-dependent separation performances of the WS_2 membranes. Thickness of the membrane is adjusted by the volume of the WS_2 nanosheets dispersion (0.2 mg/mL), and 3 mL of such dispersion will produce a 500 nm thick WS_2 membrane. Black solid squares represent water permeance; red and blue solid squares are for the rejection of cyt *c* and EB, respectively. The rejection is calculated based on the amount of the molecules in the retentate and feed solution and re-evaluated by the permeate (see details in the Materials and Methods section).

molecules act as probes to investigate the rejection performances of the WS_2 membranes with different thicknesses. The 300 nm thick WS_2 membrane is able to block 90% EB and 96% cyt *c* molecules and presents a water permeance of 730 L/m^2·h·bar. This water permeance is much higher than 71 L/m^2·h·bar of GO membranes[23] and 243 L/m^2·h·bar of MoS_2 membranes[22] with similar rejections (Supporting Information Table S1), respectively. The WS_2 membrane with a thickness of 500 nm enables blocking of 93% EB and 98% cyt *c* (Figure S1) and has water permeance down to 450 L/m^2·h·bar. Figure 2 indicates that further increasing the thickness of the WS_2 membrane from 0.5 to 1 μm only induces 15% degradation in water permeance with less than 5% increase of EB rejection, indicating that the thickness effect is saturated.

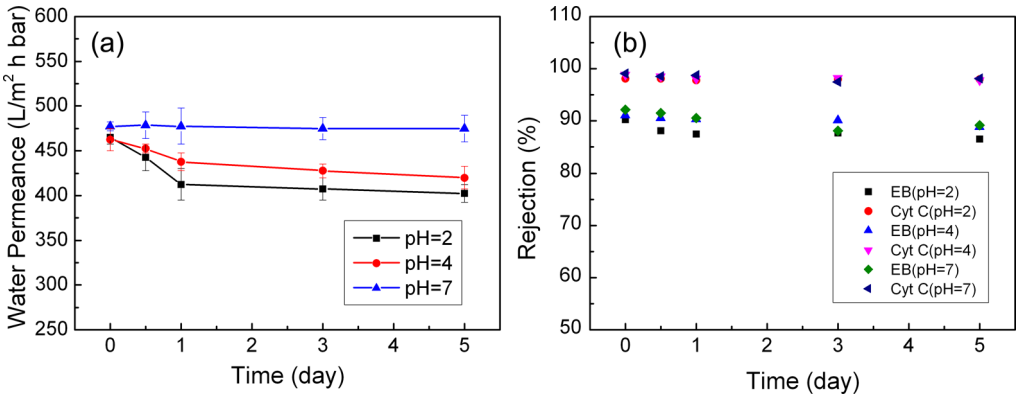

Figure 3. pH-dependent separation performances of a 500 nm thick WS_2 membrane. The separation performance is measured for 1 week, and the data are collected on 0, 0.5, 1, 3, and 5 days: (a) water permeance and (b) rejection of EB and cyt *c*.

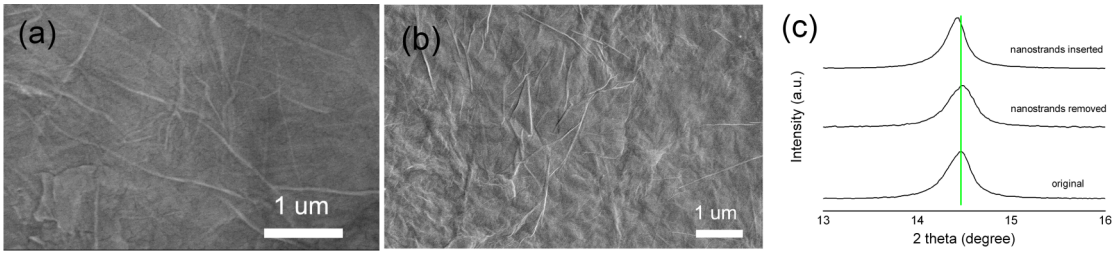

Figure 4. Overview SEM images of WS_2 membranes. (a) Inserted with ultrathin nanostrands and (b) after the nanostrands removed. (c) the XRD patterns of the as prepared, the nanostrands inserted and after removing away nanostrands WS_2 membranes, respectively.

Figure S2 shows that the concentration of EB in the retentate is obviously higher than that in the original EB feed solution. It is found that the total amount of EB from both the retentate and permeate is very close to the initial amount of EB in the feed solution. This means that the EB molecules are blocked by the WS_2 membrane instead of being absorbed. The water permeance of the 300 nm thick WS_2 membrane is 7−8 times higher than that of GO membranes with comparable rejection properties (Table S1),[11,22] demonstrating that thinner WS_2 membranes have excellent separation performance.

A 500 nm thick WS_2 membrane is used to investigate the duration and stability at different pH (Figure 3). The pH value of the feed solution is adjusted by adding diluted HCl or NaOH and monitored by a pH meter. We examine the pH-dependent separation performance consecutively in a week. Figure 3a shows that, after 12 h, at pH 2 and 4, the water permeance slightly drops by about 3.1 and 13.5%, respectively, while the water permeance in neutral solution is not changed. Zeta-potential values of WS_2 nanosheet dispersion at pH 2, 4, and 7 are less than −20 mV (Figure S3), indicating that WS_2 sheets at these pH values are negatively charged. However, the lower the pH is, the smaller the absolute value of the zeta-potential is. This means that the electrostatic repulsion force between the WS_2 sheets at lower pH are smaller than that at higher pH in the acidic range. The weakening of the electrostatic repulsion force will lead to the shrinking of the channels between the WS_2 nanosheets and finally result in reducing the water permeance. This is the reason that the water permeances at pH 2 and 4 are relatively lower than that at neutral pH. After 1 day, further decreasing of water permeance is not observed, indicating the stability of the membrane. The rejection of small molecules with different sizes through a 500 nm thick WS_2 membrane is shown in Figure 3b. Within 1 week, the rejection only decreases to less than 3% for EB and less than 1% for cyt *c*. The stable water permeation and molecule sieving performance suggest that the layered WS_2 sheets are feasible to construct an efficient separation membrane.

To further promote the separation efficiency, a nanostrand-channeled concept, which we recently developed to generate additional new nanochannels in GO membranes,[11] is employed here to construct new nanochannels in WS_2 membranes. The nanostrands/WS_2 nanosheet suspension is prepared by assembling negatively charged WS_2 nanosheets with positively charged ultrathin copper hydroxide nanostrands by electrostatic attraction. The composite membrane is obtained by filtering the nanostrands/WS_2 nanosheet suspension on an AAO porous membrane with 200 nm pores. To generate the new nanochannels, the nanostrands are removed by immersing the composite membrane into 0.15 M EDTA aqueous solution for 30 min followed by washing with

deionized water repeatedly. SEM images (Figure 4a) exhibit that nanostrands about 2 nm are embedded in the WS_2 membranes. Figure 4b shows the newly generated fluidic channels after nanostrand are removed. The volume ratio of nanostrand solution (0.7 mM)[11] and WS_2 suspension (0.2 mg/mL) is critical to get high separation performance membranes. Various volume ratios of nanostrand solution to WS_2 suspension were tried and found that the optimum volume ratio of WS_2 suspension to nanostrand solution is 5:1. Figure 4c shows XRD patterns recorded from the membranes prepared from 3 mL (0.2 mg/mL) WS_2 nanosheet suspension and 0.6 mL nanostrand solution. The shift of the WS_2 (002) peak to lower angle, equivalent to the expanding interspace between the sheets, confirms the insertion of nanostrands into the interspace of the WS_2 nanosheets. After removing the nanostrands by EDTA solution, the peak is shifted to higher angle but still lower than that of the as-prepared WS_2 membrane. This confirms that additional fluidic channels are generated, which lead to the increment of the water permeance after removing nanostrands. The corresponding XPS spectrum of nanostrands/WS_2 composite films (Figure S4a) demonstrates that copper hydroxide nanostrands are successfully inserted. The disappearance of the copper peaks in Figure S4b indicates that the nanostrands are fully removed by EDTA.

Figure 5 shows that the as-prepared (*i.e.*, nonchanneled) 500 nm thick WS_2 membrane exhibits a water permeance of 450 $L/m^2 \cdot h \cdot bar$ and 93% rejection for EB and 98% for cyt *c*. After nanostrands were inserted, the water permeance reaches 1380 $L/m^2 \cdot h \cdot bar$, while the rejection rate for EB and cyt *c* are degraded by 32 and 23%, respectively, due to the bigger channels created by the overlapped nanostrands. However, after removing the nanostrands, the nanostrand-channeled membrane demonstrates a water permeance of 930 $L/m^2 \cdot h \cdot bar$, which is double that of the as-prepared WS_2 membrane. It is exciting that the rejection of EB and cyt *c* is significantly recovered to 83 and 91%, respectively, after removing the nanostrands. This result indicates that the new nanochannels are successfully constructed by the nanofibrous templates. Compared with commercial membranes, these nanostrand-channeled WS_2 membranes have 2 orders of magnitude higher separation performances with similar rejections.[11]

To estimate the size of the fluidic channels in the WS_2 membranes, the separation performance of the membranes for molecules with different sizes was carried out. The water permeance and rejection rate of EB, cyt *c*, $K_4Fe(CN)_6$, and 5 nm gold nanoparticles solutions are recorded and summarized in Table 1. Nearly 100% gold nanoparticles are excluded by both the as-prepared and nanostrand-channeled WS_2 membranes, while only 41 and 33% of $K_4Fe(CN)_6$ are rejected by them, respectively. The permeance of the molecular solutions is relatively smaller than that of pure water due to both charge effect and interface concentration polarity. This is usually observed in the nanoseparation membranes.[11,17] The size-dependent exclusion indicates that the channels newly created have a diameter between 2 and 4 nm. Ferry's equation can be used to estimate the size of nanochannels or pores that the molecules pass across.[29] Based on the rejection and size of EB and cyt *c*, the size of the nanochannels produced by the nanostrands is estimated to be 3.83 nm, in agreement with the 100% rejection for 5 nm gold nanoparticles.

Pressure loading experiment (Figure 6) offers more information about the fluidic channels in the as-prepared and channeled WS_2 membranes. The water flux of the as-prepared WS_2 membrane linearly depends on pressure (top panel in Figure 6a). Since the corrugations are responsible for the water permeation through the as-prepared WS_2 membranes, according to the Hagen−Poiseuille equation, the linear increase of water flux with the pressure indicates a viscous flow in these channels.[11,23,29,32] This further indicates these corrugations are rigid enough to resist the external

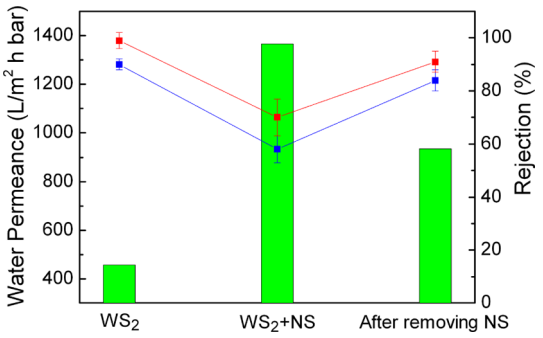

Figure 5. Separation performance of WS_2 membranes (with a thickness of 500 nm): as-prepared, inserted with nanostrands (NS), and after removing nanostrands. Columns are the water permeance, red line and blue line are the rejection of cyt *c* and EB, respectively. Error bars come from the data recorded from three individual membranes.

TABLE 1. Separation Performance of the Molecules with Different Diameters through the As-Prepared, Nanostrand-Channeled WS_2 Membranes Prepared from the Same 3 mL (0.2 mg/mL) WS_2 Nanosheet Suspension

molecule	EB	cyt *c*	$K_4Fe(CN)_6$	Au
M_W (g/mol)	961	12800	212	N/A
size (nm × nm)	1.2 × 3.1	2.5 × 3.7	0.9	5
concentration	15 μM	10 μM	1.5 mM	N/A
permeance[a] (as-prepared) ($L/m^2 \cdot h \cdot bar$)	331 ± 24	346 ± 19	317 ± 32	355 ± 12
rejection (as-prepared) (%)	92 ± 3	97 ± 1	41 ± 11	99 ± 0
permeance[a] (channeled) ($L/m^2 \cdot h \cdot bar$)	704 ± 31	725 ± 26	712 ± 45	747 ± 18
rejection (channeled) (%)	82 ± 4	91 ± 2	33 ± 13	97 ± 1

[a] The data in this row are the permeance of the solution containing corresponding molecules.

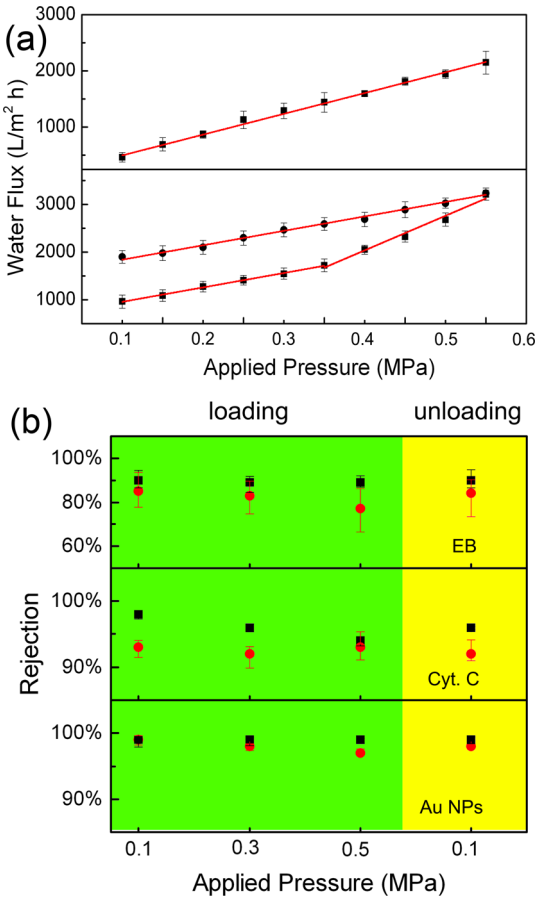

Figure 6. Pressure loading−unloading tests for the separation performance of as-prepared and channeled WS_2 membranes. (a) Water flux of as-prepared membrane (top) and channeled membrane (bottom). (b) EB, cyt *c*, and Au nanoparticle rejection: black squares and red solid circles are for the rejection rate of corresponding molecules in as-prepared and channeled membranes during pressure loading (green area) and unloading back to 0.1 MPa (yellow area), respectively. Error bars of water flux and rejection rate come from measurements of three individual membranes. The rejection rate of corresponding molecules is collected at 0.10, 0.25, and 0.50 MPa (the first three data in green area of b) during the pressure loading, while measured when the pressure is released to 0.10 MPa (the last data in yellow area of b).

pressure at least up to 0.55 MPa. The as-prepared WS_2 membrane also demonstrates stable rejection rates of EB, cyt *c*, and gold nanoparticles at different pressures (black squares shown in Figure 6b). The nanostrand-channeled WS_2 membrane displays a rather different pressure-dependent water flux. At lower pressure range, similar to the as-prepared membranes, the water flux increases linearly with external pressure. However, at 0.3 MPa, a transition of water flux with respect to pressure is observed. The flux at the external pressure above 0.3 MPa is fitted with a straight line with larger slope. The transition implies a geometry evolution of the nanochannels during the pressure loading on the channeled membranes beyond 0.3 MPa. When the external pressure is released, the water flux decreases linearly. It is worth noting that, when the pressure returns back to 0.1 MPa, the water flux of the channeled membranes is about double that of the as-prepared membrane. The larger water flux at higher pressure may be attributed to two reasons: (1) large cracks or pinholes are produced in the membranes during water passing, which is not expected; (2) new fluidic channels are built. To confirm whether the channeled membrane is broken at high pressure, the rejection rate of EB, cyt *c*, and gold nanoparticles at different pressure are investigated and compared with those of the as-prepared membrane (Figure 6b). No obvious degradation of the rejection is observed until the external pressure increases to 0.55 MPa. When the pressure is released back to 0.1 MPa, the water flux decreases linearly with the pressure, while the rejection of the molecules is retained and is close to those before loading the pressure. The stable and high rejections of these molecules in the pressure loading−unloading process demonstrate that the channeled membranes are not broken and are able to struggle against the high pressure. Hence, new fluidic channels created at the pressure above 0.3 MPa are suggested to be responsible for the further increased water flux. Additionally, according to the result of molecule exclusion, we estimate that the size of the new channels is no more than 4 nm.

On the basis of the pressure-dependent water permeation behavior, we speculate that the new fluidic channels likely originate from the cracks of the nanochannels generated by nanostrands. In the channeled membranes, both the irregular corrugations of original WS_2 nanosheets and the regular nanochannels produced by the nanostrands serve as the fluidic channels. At 0.3 MPa, the top of the channels that the nanostrands generated is suddenly cracked and responsible for the increment of water flux. In the bottom panel of Figure 6a, a straight line is well fitted with the water flux during the pressure unloading, indicating that no new cracks are produced. Moreover, high and stable rejection for small molecules of the membranes in the loading−unloading cycle demonstrates that the channeled membranes with the cracks have good mechanical properties and separation performance.

To elucidate the formation mechanism of the cracks, theoretical simulations are performed to probe the mechanical stability of the irregular corrugations in the WS_2 membranes and the regular nanochannels generated by nanostrands. First, the intrinsic mechanical properties of a 2D WS_2 crystal are quantified here by performing density functional theory (DFT)-based first-principles calculations. The Young's modulus for the WS_2 monolayer is calculated to be Y = 200 GPa, comparable to stainless steel. These results are in agreement with previous reports.[25] The in-plane tensile and compressive strengths are 19.1 and −71.3 GPa, displaying brittle behaviors, while it breaks at failure strains of 19.5 and 18.3%, respectively. Based on these

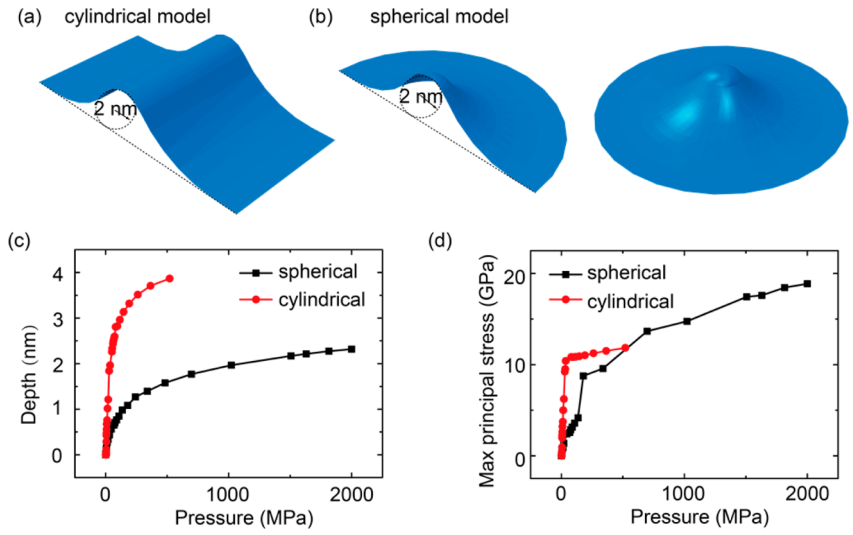

Figure 7. Finite element mechanical analysis. (a) Cylindrical and (b) half-spherical wrinkles of WS_2 membranes under pressure, which gives the responses in (c) changes of the wrinkle heights and (d) maximal principal (tensile) stress within the membrane.

material parameters, finite element methods are carried out to explore the responses of the WS_2 nanochannel under pressure. Cylindrical (representing the regular channels created by the nanostrands) and half-spherical models (the critical form of irregular corrugations in the as-prepared WS_2 membranes) are constructed with a typical channel size $d = 4$ nm, as shown in Figure 7a,b. The material is modeled as isotropic elastic with a Poisson's ratio $\nu = 0.3$. Under pressure, both cylindrical and spherical channels could buckle and the critical pressure is estimated to be $Y(2t/d)^3/4(1-\nu^2)$ and $2Y(2t/d)^2/\sqrt{3}(1-\nu^2)$, where t is the membrane thickness. With $d = 4$ nm and $t = 0.62$ nm, the critical pressure is 1.64 and 27.40 GPa, which shows remarkable geometrical enhancement in spherical shells in the elastic deformation regime and explains the observed collapse of cylindrical channels. The simulation results also show that undevelopable geometry of the spherical channel significantly enhances its stiffness (Figure 7c). Moreover, the maximal principal stress σ_p in the membrane that defines the brittle failure criteria compared to the material strength σ_b is significantly higher in the cylindrical channel when the same pressure is applied. Thus, if high pressure is loaded, the material could fail by nucleating cracks, preferentially in the cylindrical regular channels. It should be noted here that the difference in the order of magnitude of the critical pressure may arise from the presence of defects and structural disorders in the WS_2 sheet, as well as nonlinear elastic behavior that deviates from our linear constitutive assumption in modeling. Theoretical calculation indicates that, beyond the material strength, the new regular channels tend to crack under high pressure but the irregular corrugations featuring higher mechanical resistance do not. Since the separation performance under pressure of the as-prepared WS_2 membranes indicates their good mechanical properties of the irregular corrugation, the increased water permeance of the channeled WS_2 membrane is attributed to the formation of nanocracks, which not only increase the porosity (namely, entrance) but also shorten the transport path.

For comparison, Table S1 shows the separation performance of GO, MoS_2, WS_2, nanostrand-channeled GO, and nanostrand-channeled WS_2 membranes. Hagen–Poiseuille equation indicates that both the thinner and higher porous membrane should lead to a greater water permeance.[29,32] Among them, it is clear that WS_2 nanosheet-constructed membranes are the thinnest and demonstrate the best separation performance. In addition, in the nanostrand-channeled WS_2 membrane, the nanocracks generated under high pressure also contribute to improve the separation performance by shortening the transportation paths and increasing the number of entrances.

CONCLUSIONS

In summary, ultrathin WS_2 sheets are explored to construct novel separation membranes for size-selective separation of small molecules of about 3 nm. The as-prepared WS_2 membranes exhibit 5 times higher water permeance than GO membranes with similar rejection. The thinnest WS_2 membranes (300 nm) still enable blocking over 90% of the EB molecule with water permeance of 730 $L/m^2 \cdot h \cdot bar$. The water permeance is 2-fold enhanced by the duplicated channels using ultrathin nanostrands as templates without loss of the rejection efficiency. Pressure loading test indicates that water flow through the corrugation in the planes obeys the viscous flow law, and the fluidic channel size is not changed under pressure. A transition of water flux *versus* pressure is observed in the nanostrand-channeled membranes.

The pressure loading−unloading curve suggests that the channels arising from ultrathin nanostrands are cracked between 0.3 and 0.4 MPa. It is exciting that the crack produces new fluidic nanochannels and further results in water flux 4 times that of the as-prepared WS_2 membrane without degradation of the rejection performance. These WS_2 membranes have 2 orders of magnitude higher separation performances than that of commercial membranes with similar rejections and hold promising potential for highly efficient liquid separation.

MATERIALS AND METHODS

Preparation of Chemically Exfoliated WS_2 Sheets and Layered WS_2 Nanosheet Membranes[19,30]**.** In a N_2-filled glovebox, 300 mg of WS_2 powder (Alfa Aesar) is dispersed in 3 mL of 1.6 M *n*-butyllithium hexane solution (Sigma-Aldrich) under moderate stirring for 48 h. After adding several milliliters of hexane, the reaction container is removed from the glovebox. The product is collected by vacuum filtration and further washed by copious amounts of hexane. The as-received hygroscopic product is dispersed ultrasonically in 100 mL of deionized water for 60 min. The dispersion is centrifuged repeatedly, and the product is collected and redispersed in water (0.2 mg/mL) to be used for membrane preparation. The WS_2 membrane is assembled by vacuum filtration of the WS_2 dispersion on a porous anodic alumina oxide (AAO) membrane (Whatman) with a pore size of 200 nm. The thickness of the membrane is controlled by the volume of the dispersion. In our experiment, 3 mL of 0.2 mg/mL WS_2 solution leads to the membrane of about 500 nm thickness.

Copper Hydroxide Nanostrands Are Obtained *via* Our Previous Protocols[31,32]**.** Equal volumes of 4 mM copper nitrate (Sigma-Aldrich) and 1.4 mM aminoethanol (Sigma-Aldrich) aqueous solution are mixed under strong stirring for about 1 min and then left to stand for 48 h at room temperature (20−25 °C). The concentration of copper hydroxide nanostrands in the solution is about 0.7 mM.

Nanostrand-Channeled WS_2 Nanosheet Membranes. The negatively charged WS_2 nanosheets are assembled with the positively charged ultrathin copper hydroxide nanostrands by electrostatic attraction. The composite membranes are obtained by filtering the nanostrands/WS_2 nanosheet suspension on an AAO porous membrane with 200 nm pores. The volume ratio of nanostrands and WS_2 suspension with defined concentration is critical to the formation and separation performance of the membranes. The recommended experimental volume ratio of WS_2 (0.2 mg/mL) and nanostrand solution is 5:1. To generate the new nanochannels, the nanostrands are removed by immersing the composite membrane into a 0.15 M EDTA (Alfa-Aesar) aqueous solution for 30 min followed by washing with deionized water repeatedly.

Characterization. The overview and cross-section images of the membrane are captured by a field emission scanning electron microscopy (SEM, HITACHI S4800). Powder X-ray diffraction (XRD) by using graphite-monochromated Cu Kα radiation performed on an X'Pert/PRO system. XPS (X-ray photoelectron spectroscopy) analysis of the samples is carried out using Escalab 250Xi XPS spectrometer. The ultraviolet−visible (UV−vis) absorbance spectra are collected from Agilent UV 3600 spectroscopy.

Separation Performance. The filtration experiment is carried out on a standard dead-end filtration setup. The pressure-dependent filtration experiment is performed on a 25 mm high-pressure holder (Millpore Corp., Billerica, USA). The rejection rate is calculated by dividing the amount of the examined molecules in the retentate (or permeate) to its original amount in the feed solution, using following equation: $C_{retentate} \times V_{retentate}/C_{feed} \times V_{feed}$ (or $1 - C_{permeate} \times V_{permeate}/C_{feed} \times V_{feed}$) (where C is the concentration, V is the corresponding volume), the concentration of molecules is monitored by UV−vis spectroscopy; the corresponding volume was recorded by balance since the molecule concentration is very low; the solution density is very close to that of pure water. The rejection rate calculated from permeate and retentate is very consistent. Therefore, all of the rejection rates presented in the article were calculated from the retentate. The flux was calculated based on the amount of the collected permeate within certain separation processing duration. Potassium hexacyanoferrate(III) ($K_4[Fe(CN)_6]$) was purchased from J&K Inc., and 5 nm gold nanoparticle solutions were obtained from BBI. Data were measured by three individual membranes.

Calculation of the Mechanical Strength and Response to External Pressure of WS_2 Membranes. The mechanical properties of the WS_2 flakes are quantified by performing DFT-based first-principles calculations. We use the plane-wave code Vienna *ab initio* simulation package with an energy cutoff of 360 eV.[33] The projector-augmented wave potential[34] is used for the ion−electron interaction, and the Perdew−Burke−Ernzerhof (PBE) parametrization of generalized gradient approximation is implemented for the exchange-correlation functional.[35] These settings have been verified to achieve a total energy convergence for the systems under exploration below 1 meV/atom. Finite element methods are used to explore the mechanical response of wrinkled channels under pressure. A cylinder represents the regular channels created by the nanostrands, and a sphere is modeled for the critical form of irregular corrugations in the as-prepared WS_2 membranes. The diameter of bottom surface of the cylinder is consistent with a typical channel size $d = 4$ nm. The 4 nm diameter of sphere is also defined.

Conflict of Interest: The authors declare no competing financial interest.

Acknowledgment. This work is supported from the National Natural Science Foundations of China (NSFC 21271154, 11222217) and Natural Science Foundation for Outstanding Young Scientist of Zhejiang Province (LR14E020001).

Supporting Information Available: UV−vis spectra of EB and cyt *c* collected from retentate and permeate solution, UV−vis spectra of the feed, retentate, and permeate of EB passing through WS_2 at 70 min, zeta-potential of colloidal WS_2 sheet solution, XPS spectra of the membrane with ultrathin nanostrands and after the nanostrands are removed, and separation performance of different membranes (Table S1). This material is available free of charge *via* the Internet at http://pubs.acs.org.

REFERENCES AND NOTES

1. Pendergast, M. M.; Hoek, E. M. V. A Review of Water Treatment Membrane Nanotechnologies. *Energy Environ. Sci.* **2011**, *4*, 1946–1971.
2. Gin, D. L.; Noble, R. D. Designing the Next Generation of Chemical Separation Membranes. *Science* **2011**, *332*, 674–676.
3. Shannon, M. A.; Bohn, P. W.; Elimelech, M.; Georgiadis, J. G.; Marinas, B. J.; Mayes, A. M. Science and Technology for Water Purification in the Coming Decades. *Nature* **2008**, *452*, 301–310.
4. Yampolskii, Y. Polymeric Gas Separation Membranes. *Macromolecules* **2012**, *45*, 3298–3311.
5. De Baerdemaeker, T.; De Vos, D. Gas Separation Trapdoors in Zeolites. *Nat. Chem.* **2013**, *5*, 89–90.
6. Lu, W. G.; Yuan, D. Q.; Zhao, D.; Schilling, C. I.; Plietzsch, O.; Muller, T.; Brase, S.; Guenther, J.; Blumel, J.; Krishna, R.; *et al.* Porous Polymer Networks: Synthesis, Porosity, and Applications in Gas Storage/Separation. *Chem. Mater.* **2010**, *22*, 5964–5972.
7. Li, J. R.; Sculley, J.; Zhou, H. C. Metal−Organic Frameworks for Separations. *Chem. Rev.* **2012**, *112*, 869–932.
8. Nair, R. R.; Wu, H. A.; Jayaram, P. N.; Grigorieva, I. V.; Geim, A. K. Unimpeded Permeation of Water through

Helium-Leak-Tight Graphene-Based Membranes. *Science* **2012**, *335*, 442–444.
9. Joshi, R. K.; Carbone, P.; Wang, F. C.; Kravets, V. G.; Su, Y.; Grigorieva, I. V.; Wu, H. A.; Geim, A. K.; Nair, R. R. Precise and Ultrafast Molecular Sieving through GrapheneOxide Membranes. *Science* **2014**, *343*, 752–754.
10. Qiu, L.; Zhang, X. H.; Yang, W. R.; Wang, Y. F.; Simon, G. P.; Li, D. Controllable Corrugation of Chemically Converted Graphene Sheets in Water and Potential Application for Nanofiltration. *Chem. Commun.* **2011**, *47*, 5810–5812.
11. Huang, H. B.; Song, Z. G.; Wei, N.; Shi, L.; Mao, Y. Y.; Ying, Y. L.; Sun, L. W.; Xu, Z. P.; Peng, X. S. Ultrafast Viscous Water Flow through Nanostrand-Channelled Graphene Oxide Membranes. *Nat. Commun.* **2013**, *4*, 3979.
12. Chhowalla, M.; Shin, H. S.; Eda, G.; Li, L. J.; Loh, K. P.; Zhang, H. The Chemistry of Two-Dimensional Layered Transition Metal Dichalcogenide Nanosheets. *Nat. Chem.* **2013**, *5*, 263–275.
13. Wang, Q. H.; Kalantar-Zadeh, K.; Kis, A.; Coleman, J. N.; Strano, M. S. Electronics and Optoelectronics of Two-Dimensional Transition Metal Dichalcogenides. *Nat. Nanotechnol.* **2012**, *7*, 699–712.
14. Radisavljevic, B.; Radenovic, A.; Brivio, J.; Giacometti, V.; Kis, A. Single-Layer MoS_2 Transistors. *Nat. Nanotechnol.* **2011**, *6*, 147–150.
15. Lopez-Sanchez, O.; Lembke, D.; Kayci, M.; Radenovic, A.; Kis, A. Ultrasensitive Photodetectors Based on Monolayer MoS_2. *Nat. Nanotechnol.* **2013**, *8*, 497–501.
16. Mak, K. F.; He, K. L.; Shan, J.; Heinz, T. F. Control of Valley Polarization in Monolayer MoS_2 by Optical Helicity. *Nat. Nanotechnol.* **2012**, *7*, 494–498.
17. Hwang, H.; Kim, H.; Cho, J. MoS_2 Nanoplates Consisting of Disordered Graphene-like Layers for High Rate Lithium Battery Anode Materials. *Nano Lett.* **2011**, *11*, 4826–4830.
18. Kibsgaard, J.; Chen, Z. B.; Reinecke, B. N.; Jaramillo, T. F. Engineering the Surface Structure of MoS_2 To Preferentially Expose Active Edge Sites for Electrocatalysis. *Nat. Mater.* **2012**, *11*, 963–969.
19. Voiry, D.; Yamaguchi, H.; Li, J. W.; Silva, R.; Alves, D. C. B.; Fujita, T.; Chen, M. W.; Asefa, T.; Shenoy, V. B.; Eda, G.; *et al.* Enhanced Catalytic Activity in Strained Chemically Exfoliated WS_2 Nanosheets for Hydrogen Evolution. *Nat. Mater.* **2013**, *12*, 850–855.
20. Perkins, F. K.; Friedman, A. L.; Cobas, E.; Campbell, P. M.; Jernigan, G. G.; Jonker, B. T. Chemical Vapor Sensing with Monolayer MoS_2. *Nano Lett.* **2013**, *13*, 668–673.
21. Nicolosi, V.; Chhowalla, M.; Kanatzidis, M. G.; Strano, M. S.; Coleman, J. N. Liquid Exfoliation of Layered Materials. *Science* **2013**, *340*, 1420.
22. Huang, H. B.; Mao, Y. Y.; Ying, Y. L.; Liu, Y.; Sun, L. W.; Peng, X. S. Salt Concentration, pH and Pressure Controlled Separation of Small Molecules through Lamellar Graphene Oxide Membranes. *Chem. Commun.* **2013**, *49*, 5963–5965.
23. Sun, L. W.; Huang, H. B.; Peng, X. S. Laminar MoS_2 Membranes for Molecule Separation. *Chem. Commun.* **2013**, *49*, 10718–10720.
24. Chen, H.; Muller, M. B.; Gilmore, K. J.; Wallace, G. G.; Li, D. Mechanically Strong, Electrically Conductive, and Biocompatible Graphene Paper. *Adv. Mater.* **2008**, *20*, 3557–3561.
25. Lee, C.; Wei, X. D.; Kysar, J. W.; Hone, J. Measurement of the Elastic Properties and Intrinsic Strength of Monolayer Graphene. *Science* **2008**, *321*, 385–388.
26. Bertolazzi, S.; Brivio, J.; Kis, A. Stretching and Breaking of Ultrathin MoS_2. *ACS Nano* **2011**, *5*, 9703–9709.
27. Ghorbani-Asl, M.; Borini, S.; Kuc, A.; Heine, T. Strain-Dependent Modulation of Conductivity in Single-Layer Transition-Metal Dichalcogenides. *Phys. Rev. B* **2013**, *87*, 235434.
28. Li, T. S. Ideal Strength and Phonon Instability in Single-Layer MoS_2. *Phys. Rev. B* **2012**, *85*, 235407.
29. Karan, S.; Samitsu, S.; Peng, X. S.; Kurashima, K.; Ichinose, I. Ultrafast Viscous Permeation of Organic Solvents through Diamond-like Carbon Nanosheets. *Science* **2012**, *335*, 444–447.
30. Eda, G.; Yamaguchi, H.; Voiry, D.; Fujita, T.; Chen, M. W.; Chhowalla, M. Photoluminescence From Chemically Exfoliated MoS_2. *Nano Lett.* **2011**, *11*, 5111–5116.
31. Peng, X. S.; Jin, J.; Ericsson, E. M.; Ichinose, I. General Method for Ultrathin Free-Standing Films of Nanofibrous Composite Materials. *J. Am. Chem. Soc.* **2007**, *129*, 8625–8633.
32. Peng, X. S.; Jin, J.; Nakamura, Y.; Ohno, T.; Ichinose, I. Ultrafast Permeation of Water through Protein-Based Membranes. *Nat. Nanotechnol.* **2009**, *4*, 353–357.
33. Giannozzi, P.; Baroni, S.; Bonini, N.; Calandra, M.; Car, R.; Cavazzoni, C.; Ceresoli, D.; Chiarotti, G. L.; Cococcioni, M.; Dabo, I.; *et al.* QUANTUM ESPRESSO: A Modular and Open-Source Software Project for Quantum Simulations of Materials. *J. Phys.: Condens. Matter* **2009**, *21*, 395502.
34. Kresse, G.; Joubert, D. From Ultrasoft Pseudopotentials to the Projector Augmented-Wave Method. *Phys. Rev. B* **1999**, *59*, 1758–1775.
35. Perdew, J. P.; Burke, K.; Ernzerhof, M. Generalized Gradient Approximation Made Simple. *Phys. Rev. Lett.* **1996**, *77*, 3865–3868.